Preparation and Characterization of Cerium Doped YAG Nanoparticles

by

Jing Cai

(Under the direction of William M. Dennis)

Abstract

The research presented in this thesis focuses on the characterization of Cerium doped Yttrium Aluminum Garnet (YAG:Ce^{3+}) nanoparticles prepared by gas phase condensation. The nanoparticles were characterized using scanning electron microscopy (SEM), atomic force microscopy (AFM) and optical spectroscopy techniques. SEM and AFM measurements reveal that the mean diameter of the nanoparticles were 27 ± 4 and 38 ± 5 nm. The excitation and emission spectra of the nanoparticles were very similar to the spectra of the bulk single crystal YAG:Ce^{3+} indicating that YAG:Ce^{3+} nanocrystals had been successfully prepared. The effect of finite size on spectral peak position was investigated.

Index words: YAG:Ce^{3+}, Nanoparticles, Scanning Electron Microscopy, Atomic Force Microscopy, Optical Spectra, Finite Size Effects

Preparation and Characterization of Cerium Doped YAG Nanoparticles

by

Jing Cai

B.S., Lanzhou University, China 1998

A Thesis Submitted to the Graduate Faculty
of The University of Georgia in Partial Fulfillment
of the
Requirements for the Degree

Master of Science

Athens, Georgia

2002

© 2002

Jing Cai

All Rights Reserved

Preparation and Characterization of Cerium Doped YAG Nanoparticles

by

Jing Cai

Approved:

Major Professor: William M. Dennis

Committee: Uwe Happek
Michael R. Geller

Electronic Version Approved:

Gordhan L. Patel
Dean of the Graduate School
The University of Georgia
August 2002

Acknowledgments

This thesis would not exist without the efforts and kindness of many people. First, I would like to extend my deepest gratitude my advisor, Dr. William M. Dennis, whose guidance, support and patience have helped me greatly all the way through this project. I am full of appreciation to my two other committee members, Dr. Michael R. Geller and Dr. Uwe Happek. To these respected professors, I am and shall forever remain grateful.

I would like to extend my sincere thanks to Carl Liebig, for providing invaluable information on the experiment. Without his knowledge and kindness in sharing, the project would be far more difficult. And I thank my fellow physics graduate students Jianwei Wang, Paul Schmidt, Steve Cox, Jay Fleniken, Hairong Zheng, for giving candid feedback and sincere suggestions for improvement.

I thank my dearest friend, juanjuan, who has enriched my life in more ways that I can express. I am indebted to my friends, in the U.S. and back in China, especially to Xiao You, Lao Du, Qing Qiang, Luo Lu, Xiao Fang and Dabao, for their warm support, even at times when difficulties seem overwhelming.

The thesis is also to my parents and brother, who are as close to me as ever, although far away in China.

It is to them that this thesis is dedicated.

Table of Contents

List of Figures

List of Tables

Chapter 1

Introduction

To date there has been a considerable body of work on rare–earth doped insulators. These materials often find application as phosphors, scintillators, laser materials and optical amplifiers, and have been explored for such applications as optical memories and processors[1].

Cerium, with the electronic configuration of $[Xe]4f^26s^2$, is one of the most commonly used rare earth ions used to activate insulating materials. Trivalent cerium Ce^{3+} is described by a single electron–system with the electronic configuration $[Xe]4f^1$. The application of Ce^{3+} as the activator in phosphors, scintillators and laser materials has attracted considerable attention starting from the early days of phosphor–related research. Study on the fluorescence of cerium–activated compounds was first performed in the early of 1950s and there has been continuous activity since that time. As a consequence, Ce^{3+} has been studied in a wide range of hosts including liquids, amorphous inorganic and organic systems, ceramics, and a large number of crystalline materials. Among the publications on scintillator materials currently investigated, Cerium outnumbers any other ion used to activate solid state materials[2]. Due to the electronic configuration of Ce^{3+}, a single $4f$–electron, the cerium–activated compounds generally exhibit high light yield, favorable UV or blue emission, fast fluorescence decay time, and temperature stability; this makes Ce^{3+} attractive for applications such as scintillator materials, phosphors, and laser applications. The physical and optical properties of YAG:Ce^{3+} are summarized in Table 1.1.

Table 1.1: Physical and optical properties of YAG:Ce^{3+} crystals, data from Ref. [3].

Physical Properties		Luminescence Properties	
Density (g/cm^3)	4.57	Wavelength of peak emission (cm^{-1})	19042
Index of refraction	1.82	Decay constant (ns)	70
Crystal structure	Cubic	Radiation length (cm)	3.5
Melting point (^{o}C)	1970	Photon yield at 300K (10^3 Ph/MeV)	8

Compared with bulk crystalline YAG:Ce^{3+}, nanoscale YAG:Ce^{3+} materials have not yet been widely studied. Nanoparticles and nanoclusters are a new class of materials that often exhibit unique chemical and physical properties when compared with their bulk counterparts. In addition, they can have improved qualities with respect to use in various optical, electrical, mechanical, magnetic and catalytic applications[4]. The optical and electronic properties of nanoparticles with controlled size and shape have attracted widespread interest in the scientific community. One of the two major concerns of this thesis is the reported spectral shift which has been attributed to finite size effects in nanoscale YAG:Ce^{3+}[5].

Doped insulating nanoparticles provide an ideal model system for the investigation of the electron-lattice interaction in nanoscale systems. The insulating host eliminates the complications that arise from collective electron effects, while the dopant ions provide a simple electronic level system. The nanoscale rare–earth–doped systems can be categorized according to whether the electronic states of the impurity are weakly or strongly coupled with the modes of nanoparticles. Y_2O_3:Eu^{3+} and YAG:Ce^{3+} provide examples of weakly and strongly coupled systems respectively[6][7]. In this work, nanoparticles of YAG:Ce^{3+} were prepared and

characterized. The YAG:Ce^{3+} nanoparticles used in this study were prepared using a cw–CO_2–laser–heated evaporation/condensation method[8] and to our knowledge, this is the first attempt to prepare these nanoparticles using this technique.

The resulting nanoparticles were characterized using scanning electron microscopy, atomic force microscopy, and optical spectroscopic techniques. Two samples of YAG:Ce^{3+} nanoparticles were used in this study, while another two samples, a single crystal and a fused crystalline bulk material, were also studied for the purpose of comparison since the properties of single crystal YAG:Ce^{3+} have already been thoroughly characterized. The results in the thesis are compared with results from the literature on nanoscale YAG:Ce^{3+} prepared by the polyacrylamide gel technique[5].

The objectives of this thesis involve the preparation, characterization and visible and UV excitation and emission spectra of Cerium-doped YAG nanoparticles. The thesis is organized as follows:

Chapter two reviews the techniques of scanning electron microscopy (SEM) and atomic force microscope (AFM) which are used to characterize the nanoparticles studied in this thesis. The fundamental concepts of crystal field theory are reviewed and its application to YAG:Ce^{3+} spectra discussed. Finally a review of the transient dynamics of YAG:Ce^{3+} is presented.

Chapter three is concerned with the preparation and characterization of YAG:Ce^{3+} nanoparticles. The gas phase condensation process used to prepare the nanoparticles is introduced at the beginning of this chapter, as well as the laser heated pedestal growth (LHPG) technique used to grow the single crystal fiber. Results obtained using scanning electron microscope (SEM) and atomic force microscope(AFM) are presented, and the size distribution is then determined based on the information obtained from the images. Emission and excitation spectra of

YAG:Ce^{3+} nanoparticles are measured and compared with the spectra of the bulk materials, and results from the literature[5].

The conclusions of this thesis are presented in Chapter four.

1.1 References

[1] B. Henderson, and G. F. Imbusch, *Optical Spectroscopy of Inorganic Solids*, (Clarendon Press, Oxford, 1989).

[2] S. E. Derenzo, W. W. Moses, M. J. Weber, A. C. West, in scintillator and Phospher Materials, eds. M. J. Weber, P. Lecoq, R. C. Ruchti, C. Woody, W. M. Yen and R. Y. Zhu, ,Materials Research Society Symposium Proceedings, **348**, (1994) 39.

[3] A. Murokh, J. Rosenzweig, V. Yakimenko, E. Johnson and X. J. Wang, World Scientific, (2000).

[4] G. Blasse, J. Alloys Compounds, **225**, (1995) 529.

[5] Q. Li, L. Gao and D. Yan, Mater. Chem. & Phys., **10**, (1998) 2837–2845.

[6] H. Yang, S. P. Feofilov, D. K. Williams, J. C. Milora, B. M. Tissue, R. S. Meltzer and W. M. Dennis, Physica B, **263-264**, (1999) 476-478.

[7] J. Yu, H. Liu, Y. Wang, W. Jia, J. Lumin., **79**, (1998) 191-199.

[8] B. M. Tissue, Chem. Mater. **10**, (1998) 2837-2845.

Chapter 2

Background Review

This chapter will address some of the techniques used to characterize the nanoparticles and their spectral properties. The size characterization of the crystals was accomplished using scanning electron and atomic force microscopies, both of which are described in this chapter. The basic concepts of crystal field theory as it pertains to the energy levels and spectra of Ce^{3+} ions in YAG are briefly reviewed. Finally, results on the transient dynamics of YAG:Ce^{3+} from the literature are summarized.

2.1 Characterization Techniques

To perform the high resolution surface investigations of the YAG:Ce^{3+} nanoparticles used in this work, two commonly used microscopies were employed. The Scanning Electron Microscope (SEM) uses electrons to probe the material while Atomic Force Microscope (AFM) uses ultra–fine tips to explore the surface of the material, each of these techniques resolves surface structure down to the nanometer scale and were used to determine the average size and size distribution of the nanoparticle materials studied in this thesis.

2.1.1 Scanning Electron Microscopy

A scanning electron microscope was used to examine the size distribution and the morphology of the YAG:Ce^{3+} nanoparticles. Unlike conventional light microscopes which use a series of lenses to focus light and create a magnified image, the SEM

creates the magnified images using a focused beam of electrons. The SEM produces a detailed three–dimensional image; due to the size of the electron wavelength it is possible to obtain higher magnifications than with optical microscopes.

The operation of the SEM consists of applying a voltage between a conductive sample and a filament, resulting in the electrons emitted from the filament being focused onto the sample. Operation occurs in a vacuum environment ranging from 10^{-4} to 10^{-10} Torr. The electrons interact with the sample from within a few nanometers to several microns from the surface, depending on the beam parameters and sample properties. The electrons are guided onto the sample by a series of electromagnetic lenses in the electron column. Samples must be prepared carefully to withstand the vacuum inside the microscope, in addition, since the SEM uses electrons, the samples must be able to conduct electricity. The sample is placed inside the microscope's vacuum column through a load–lock. After the air is pumped out of the column, an electron gun emits a beam of high energy electrons. The electron beam travels through a series of magnetic lenses designed to focus the electrons to a very fine spot. Near the bottom, a set of scanning coils moves the focused beam back and forth across the sample. As the electron beam hits each position on the sample, secondary electrons are emitted from the surface. These electrons are deflected and amplified. The final image is built up from the number of electrons emitted from each position on the sample.

2.1.2 Atomic Force Microscopy

The YAG:Ce^{3+} nanoparticles were also characterized using atomic force microscopy. AFM provides the three–dimensional surface topography with nanometer lateral and sub-angstrom vertical resolution on both insulators and conductors. An AFM typically consists of a probe attached to a spring loaded cantilever, a dye laser, and a piezo–electric scanner. AFM measurements result from the interaction of the probe

with the surface of a sample. The scanning motion is achieved using a piezo–electric tube scanner which scans the tip in a raster pattern with respect to the sample (or scans to the sample with respect to the tip). The dye laser beam is directed onto the part of the cantilever opposite the probe, the tip–sample interaction is monitored by reflecting a laser off the back of the cantilever into a split photo–diode detector. As the cantilever moves up and down, the reflected beam is deflected; therefore, the position of the tip above the sample may be associated with a deflection of the laser beam[1]. In contrast to SEM which is conducted in a vacuum environment, AFM can be performed in an ambient or fluid environment. Furthermore, SEM measurements require that the sample be conductive or have a conducting coating, AFM measurements do not have this restriction.

The two most commonly used modes of operation for the AFM are contact mode AFM and tapping mode AFM. Contact mode AFM consists of scanning the probe across a sample surface while monitoring the change in cantilever deflection with the split photo–diode detector. A feedback loop maintains a constant cantilever deflection by vertically moving the scanner to maintain a constant photo–detector difference signal. The distance the scanner moves vertically at each x, y data point is stored by the computer to form the topographic image of the sample surface. Tapping mode AFM consists of oscillating the cantilever at its resonance frequency (typically $\sim$300 kHz) and lightly tapping on the surface during scanning. The laser deflection method is used to detect the root–mean–square (RMS) amplitude of cantilever oscillation. A feedback loop maintains a constant oscillation amplitude by moving the scanner vertically at every x, y data point. Again, recording this signal as a function of position enables a topographical image to be constructed.

The advantage of tapping mode AFM over contact mode AFM is that it eliminates the lateral, shear forces present in contact mode. This enables tapping mode AFM to image soft, fragile, and adhesive surfaces without damaging them. Consid-

ering that the nanoparticle materials form soft, light powder, the tapping mode was chosen for this study.

2.2 Optical Spectroscopy

Two optical spectroscopic techniques were utilized in this thesis. (i) Excitation spectra, an excitation spectrum gives the dependence of the emission intensity on the frequency of exciting light. (ii) Emission spectra, an emission spectrum gives the dependence of the emitted intensity as a function of frequency.

In general, luminescence can be categorized into: short time emission, i.e. fluorescence and long time emission, i.e. phosphorescence. Fluorescence emission takes place simultaneously with the absorption of radiation and stops shortly after the radiation ceases. Phosphorescence is used to describe the process in which luminescence is preceded by the population residing in a meta–stable state, for example, capture of electrons by traps in semiconductors.

The processes of absorption and emission in a system with strong electron–phonon coupling can be understood using a configurational coordinate diagram, shown in Fig. 2.1. Absorption (a vertical transition) causes the center to occupy a high vibrational level in the electronic excited state. The center relaxes to the lowest vibrational level of the electronic excited state giving up the excess energy to the lattice. Another way to describe this process is to say that nuclei adjust their positions on the excited state potential energy surface, so that the nuclear configuration is in equilibrium. This process is called relaxation. During relaxation, radiative emission is very improbable. This can be understood by examining the relative relaxation rates: A dipole allowed radiative transition rate is $\sim 10^8$ s^{-1}, while typical vibrational relaxation rates are on the order of 10^{13} s^{-1}.

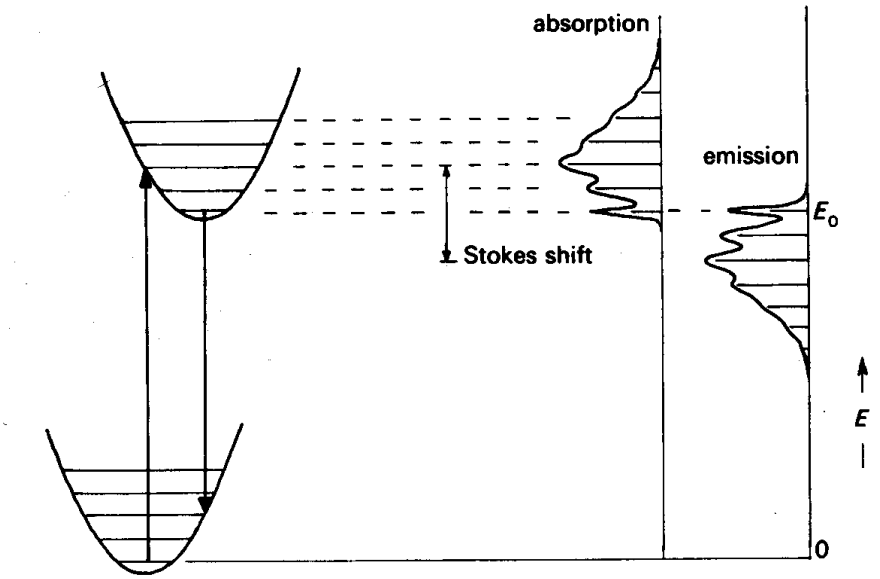

Figure 2.1: Configurational coordinate diagram. The band peaks occur at the energies given by the lengths of the vertical arrows, hence the emission band is at lower energy. The shift in energy between the absorption and emission band is known as the Stokes shift. Picture is from reference (B. Henderson and G. F. Imbusch, *Optical Spectroscopy of Inorganic Solids*, Clarendon Press, Oxford, 1989)

After emission (another vertical transition), the center occupies a high vibrational state in the electronic ground state. Again, nonradiative relaxation rapidly occurs to the lowest vibrational level of the ground state. As can be seen from the configurational coordinate diagram, the emission occurs at a lower energy than the absorption resulting in a Stokes shift.

2.3 Crystal Field Theory

Crystal field theory has been developed to describe the electronic energy levels of impurities ions doped into a host material. The addition of impurities to insulating solids leads to the generation of new optical absorption features, due to the introduction of energy states in the forbidden gap between the extended electronic states of the host lattice. The optical properties of insulating materials are foremost determined by the energy levels of the impurities. A brief description of crystal field theory, following the approach outlined by Henderson and Imbusch is given below[2].

Optical transitions involve only changes in the states of the outer electrons; the inner electrons occupying closed shells or subshells are normally unaffected by these transitions. The inner electrons therefore create a constant electrostatic central field with which the optically active electrons interact. The Hamiltonian can therefore be written:

$$H = \sum_i \frac{\vec{p}_i^2}{2m} + \sum_i V_{CF}(\vec{r}_i) + H' + H_{SO} + H_C \tag{2.1}$$

where the first term is the kinetic energy of the optically–active electrons and the second term is the potential energy due to the nucleus and inner closed shells for the ith electron. The subscript CF means central field. H' is the Coulomb interaction between optically active electrons, H_{SO} describes the spin–orbit interaction, H_C is the energy of the optically–active electrons with the electrostatic crystal field. The

simplest description of the crystal field uses the point ion model, in which ligand ions causing the electrostatic crystal field are represented by point charges.

Depending on the relative size of H_C, H_{SO} and $H^{'}$, there are three cases. (i) Weak crystal field: $H_C \ll H^{'}$, H_{SO}. (ii) Intermediate crystal field: $H_{SO} < H_C < H^{'}$. (iii) Strong crystal field: $H_{SO} < H^{'} < H_C$.

For Ce^{3+} with a single optically active electron the $4f$ states are described by the weak crystal field case while the $5d$ states are described by the strong crystal field case.

The triply–charged rare earth ions have the configuration $(1s^2 \cdots 4d^{10})4f^n 5s^2 5p^6$, $n < 14$, where the $4f$ are the optically–active electrons. The next highest configuration, $4f^{n-1}5d$, which gives rise to energy levels $40,000 - 100,000$ cm^{-1} above the $4f^n$ configuration.

The eigenstates of H_{CF} are $|(n_i l_i)\rangle$, and the eigenstates of $H_{CF} + H^{'}$ are $|(n_i l_i) L S M_L M_S\rangle$, if configuration mixing is neglected due to the large energy separation between configurations. Eigenstates of $H_{CF} + H^{'} + H_{SO}$ are $|(n_i l_i) L S J M_J\rangle$ in the Russell–Saunder approximation, where the mixing of states of different LS is neglected; this is a good approximation only if the LS energy levels are well separated.

The Coulomb interaction between the outer electrons splits the energy level of the electron configuration $(n_i l_i)$ into a number of LS terms, while the spin–orbit interaction, H_{SO}, splits each LS term into J multiplets. The electronic states of ions are noted as $^{2S+1}L_J$, where S is the spin angular momentum, L is the orbital angular momentum and J is the total angular momentum and its value varies from $|L - S|$ to $|L + S|$. In the ground state, $J = L - S$ when the shell is less than half–filled, otherwise $J = L + S$.

The optically active $4f$ electrons of the rare earth ions are shielded by the outer, though less energetic, $5s$ and $5p$ shell electrons. As a result the optically active $4f$

electrons of rare earth ions in solids are not strongly affected by neighboring ligands. If the neighboring ligands are neglected the energy levels of the $4f$ electrons are just free ion levels, characterized by L, S, J values. The azimuthal quantum number of the $4f$ shell is 3, and there are 7 orbitals in this shell. Two electrons with opposite spin are allowed in each of the orbitals. The electrons tend to have the same spin, unless the shell contains more than 7 electrons and is over half–filled. In the ground state of Ce^{3+}, which has one $4f$ electron, $S = 1/2$ and $L = 3$. H_{SO} splits the ^{2}F LS term into $J = L - S = 5/2$ and $J = L + S = 7/2$ states. Therefore the two lowest energy mainfold are denoted by $^2F_{5/2}$ and $^2F_{7/2}$. The energy state $^2F_{5/2}$ is lower than the energy state $^2F_{7/2}$ since $4f$ shell is less than half–filled.

The $5d$ orbital of Ce^{3+} is much more strongly affected by the neighboring ions, i.e., the crystal field. The crystal field experienced by a center reflects the symmetry of the environment of the center. In the case of YAG:Ce^{3+} crystal, the Ce^{3+} sits in a distorted cubic site.

2.4 Ce^{3+} Energy Level Structure

The trivalent state of Cerium has the electronic configuration [Xe]$4f^1$ that leads to a large gap of about 20,000–35,000 cm^{-1} between the lowest $5d$ orbital and the ground state, which is split into two components, $^2F_{5/2}$ and $^2F_{7/2}$, by the spin–orbit interaction, with a splitting energy gap of 2,200 cm^{-1}[3]. The fluorescence of Ce^{3+} activated compounds has been well studied[4]. Usually the emission spectrum consists of a broad band with two peaks in the near ultraviolet region.

When YAG crystals are doped with Ce^{3+}, the Ce^{3+} ion sits in a distorted cube and the 5d configuration of Ce^{3+} ion is split by the crystal field into a low energy doublet (e_g) and a higher energy triplet (t_{2g}). Fig. 2.2 illustrates the structure of Ce^{3+} ion energy levels together with band structure of the host material (YAG) as

known from the literature[5]. The primary excitation wavelengths are shown, with absorbed energy ultimately feeding the emission from the lowest $5d$ level back down to the $4f$ terminal state.

Since the energy gap between valence band (VB) and conductance band (CB) in YAG is 56,012 cm^{-1} as is illustrated in the figure, optical radiation at this or longer wavelengths will either excite (or ionize) the emitting Ce^{3+} ion[6]. The electronic structure and therefore the optical properties of the YAG:Ce^{3+} crystals are determined by the $4f$ and $5d$ electronic energy levels of Ce^{3+} ions split by the spin–orbit interaction and a crystal field of D_2 symmetry, respectively.

2.5 Decay Kinetics of YAG:Ce^{3+} Crystal

It is useful for the work described in this thesis to know the decay kinetics of Ce^{3+} in YAG. The fluorescence transients can be measured for the transition from the lowest crystal field components of the $5d$ configuration to the two $4f$ states. This gives the Ce^{3+} emission its typical double–band shape. A single exponential fluorescence transient on the nanosecond timescale is generally observed with a decay time constant of less than 100 ns. The decay time increases proportional to the wavelength squared[7]. For example, the decay time is 20 ns for the 33323 cm^{-1} emission of CeF_3 compared with 70 ns for the 18176 cm^{-1} emission of YAG:Ce^{3+}.

In a study by Weber, the decay kinetics of the YAG:Ce^{3+} crystal was measured over a broad range of temperatures, 70–770 K, under direct optical excitation of the Ce^{3+} ion[8]. Weber's findings show that up to some 600 K the decay can be expressed as a single exponential with a time constant to the range of 63–67 ns. Later measurements by Spowart *et. al.* produced the similar results[9]. Recently, E. Zych carried out a number of works on the decay dynamics of YAG:Ce^{3+} single crystal and highly dense transparent ceramic. The decay dynamics were measured

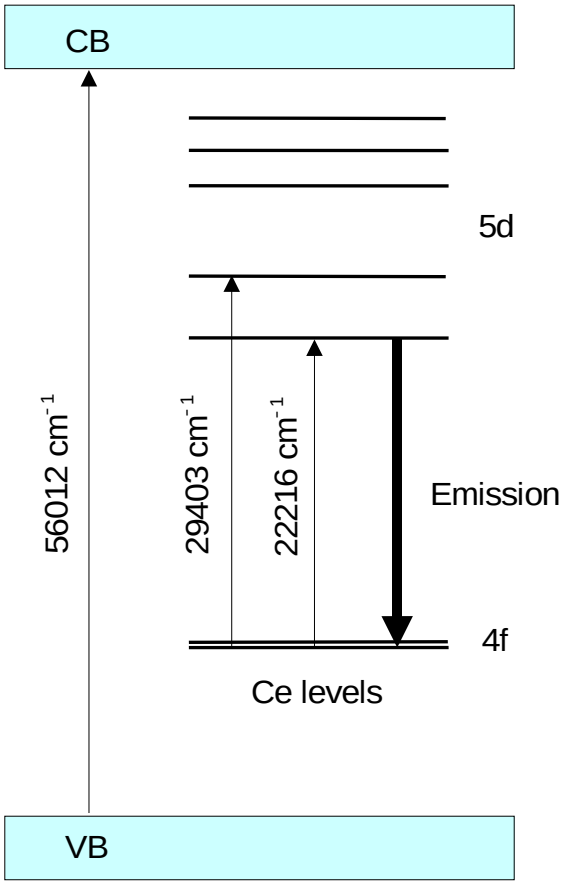

Figure 2.2: Schematic diagram of the energy levels and band structure of YAG:Ce^{3+} single crystal, the position of the Ce^{3+} ion levels within the band gap is approximate.

using both optical and ionizing excitation. His results showed that for excitation by 22216 cm^{-1} light follows a single–exponential decay pattern with a time constant of 67 ns, in accord with Weber's results.

2.6 References

[1] G. Binning, C. F. Quate and C. Gerber Phy. Rev. Lett., **56**, 9, (1986) 930-933.

[2] B. Henderson and G. F. Imbusch, *Optical Spectroscopy of Inorganic Solids*, (Clarendon Press, Oxford, 1989).

[3] G. Blasse and A. Bril, J. of Chemical Physics, 41, **12**, (1967) 5139-5145.

[4] E. Zych, C. Brecher, A. J. Wojtowicz and H. Lingertat, J. Lumin., **75**, (1997) 193-203.

[5] T. Tomiki, H. Akamine, M. Gishiken, Y. Kinjoh, M. Miyazato, N. Miyazato, M. Hiraoka, N. Hirata, Y. Ganaha and T. Futemma, J. Phys. Soc Japan, **60**, (1991) 2437.

[6] V. Murk and N. Yaroshevich, Phys.: Status Solidi b, **181**, (1994) K 37.

[7] D. B. Bartolo, *Optical interactions in solids*, (Wiley, New York, 1968).

[8] E. Zych, C. Brecher and J. Glodo J. Phys.: Condens. Matter, **12**, (2000) 1947.

[9] E. Zych, C. Brecher, A. J. Wojtowicz and H. Lingertat, J. Lumin. **75** (1997) 193.

Chapter 3

Experimental Considerations and Results

3.1 Sample Preparation

In this study YAG:Ce^{3+} was studied in both bulk and nanoparticle forms. Four samples were used in this study, two of which were collected at different places in the sample preparation chamber. Sample N1 and sample N2 were nanoparticles prepared by a gas–phase condensation method. Sample N1 was collected from the cold finger, while sample N2 was collected from the walls of the chamber. Sample B1 was a fused crystalline material formed from the melted source material; sample B2 is a single crystal fiber prepared by the laser heated pedestal growth method. In this chapter, the sample preparation processes, and growth methods, for both sets of samples are introduced. The excitation and emission spectra of the Cerium doped YAG nanoparticles are compared to the bulk YAG:Ce^{3+}, and to data from the literature, which is labeled as sample L1 in this thesis[1].

3.1.1 Preparation of Nanoparticles

The YAG:Ce^{3+} nanoparticles used in this study were prepared by B. M. Tissue and co–workers[2] by a gas phase condensation using a continuous working CO_2 laser to heat a ceramic target. To our knowledge this is the first time that Cerium doped YAG nanoparticles have been prepared using this method. Fig. 3.1 shows the apparatus and a schematic diagram for gas phase condensation using CO_2 laser heating.

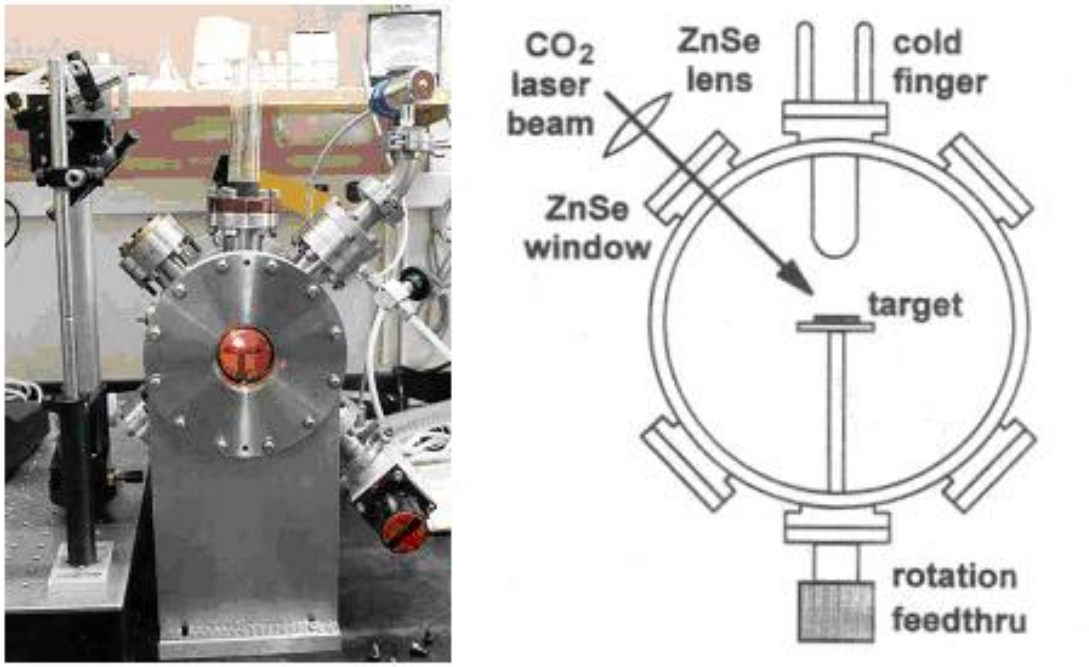

Figure 3.1: Photograph and the schematic diagram of the experimental apparatus used for the preparation of nanoparticles by gas phase condensation using CO_2 laser heating. Pictures are from H. Eilers and B. M. Tissue, Materials Letters, **24** (1995) 261-265.

In the gas phase condensation method, a CO_2 laser is used to heat the source material in an inert gas at low pressure. Clusters are formed in the gas phase and then condense on a cold finger. The particle diameters are controlled by varying vaporization conditions, such as the inert gas pressure. Starting materials for the nanoparticles YAG:Ce^{3+} were $Ce(NO_3)_3$: $6H_2O$, Al_2O_3 and Y_2O_3. The initial Ce^{3+} concentration was 0.5 Mol%, the laser power was 45W and the cold finger temperature was 60^{o}C. The inert gas was N_2 at 100 Torr. Sample N1 was the 45 mg yield on the cold finger. Sample N2 was additional material collected from the chamber walls.

3.1.2 Preparation of Bulk Materials

In order to understand the effects of the nanoscale system it is necessary to compare the results to those obtained in the bulk material. Two types of bulk material samples were prepared and studied for comparison. Sample B1 is a fused crystalline material formed from the source material during nanoparticle growth.

Sample B2 is a YAG:Ce^{3+} is a single crystal fiber, which was grown by laser heated pedestal growth method (LHPG) at the Department of Physics and Astronomy, University of Georgia (see in Fig. 3.2). LHPG is a variant of the Czochralski growth technique. Since there is no crucible or furnace required in this method, crystals grown can avoid possible contamination from the crucible and stress–induced defects caused by different thermal expansion coefficients between the crucible and the crystal. The LHPG growth method is a rapid growth technique, typically on the order of mm/min, and a steep temperature gradient, which enables the growth of materials with high melting temperatures. Note, YAG has a melting temperature of 1970 ^{o}C.

When growing a single crystal fiber, a *Synrad* 57–1 100W CO_2 laser pulsed at 5 kHz was used as the heating source. The laser beam was expanded into a large donut

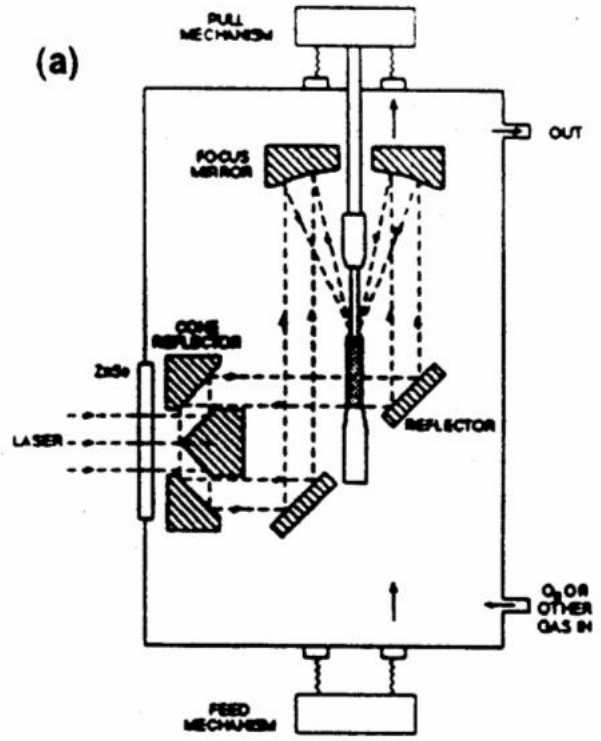

Figure 3.2: Cross sectional view of the LHPG growth area showing the Reflaxicon focusing system. Picture is from W. M. Yen, *Insulating Materials for Optoelectronics*, F. Agullo-Lopez, ed. (World Scientific, Singapore, 1998) 261-265.

and then was focused onto the source rod using a specialized set of optics denoted a reflaxicon. The laser radiation is absorbed, producing a self supporting molten bead at the top of the source rod. A seed crystal is then dipped into the melt with crystallization occurring at the seed/melt interface as the seed is pulled upwards out of the melt and away from further exposure from the CO_2 laser radiation. The surface tension of the molten bead holds the seed and the melt together and is responsible for forming the pedestal shape of the melt under the dynamics of pulling. As the material is fed into the crystallizing fiber, the source rod is simultaneously fed into the heating zone in order to maintain a constant volume of melt. If the seed is not a single crystal, the initial part of the fiber is usually a bundle of twinned crystals. However, the fiber eventually becomes a single crystal through competitive growth. The size of the resulting fiber grown using this method had the diameter of 0.8 mm and a length of 12 mm.

3.2 Surface Characterization of YAG:Ce^{3+} Nanoparticles

All samples were characterized using scanning electron microscope (SEM), atomic–force microscope (AFM). SEM and AFM were performed to determine the average size and the size distributions of the YAG:Ce^{3+} nanoparticle samples.

3.2.1 SEM Results

The average particle size and size distribution of YAG:Ce^{3+} nanoparticles, for both sample N1 and sample N2, were characterized using a scanning electron microscope (SEM). In particular, a LEO 982 field emission scanning electron microscope in the secondary emissive mode was used for the purpose of achieving ultra high resolution images. Samples were prepared for SEM measurements by sprinkling and crushing

the nanoparticles powers on a carbon–coated adhesive bar. A high vacuum evaporator, Model Denton DV502A, was then used for fine carbon evaporation of the samples. Fig. 3.3 shows a SEM image of sample N1. From the SEM results it is clear that the YAG:Ce^{3+} nanoparticles deviate from a perfectly spherical geometry and form clusters. Distinct nanoparticles could be easily seen as well in the image. By counting the number of distinct particles with the same size, the size distribution of sample N1 was obtained and presented in the histogram shown in Fig. 3.4. The histogram reveals that nanoparticles have a broad size distribution between 25 and 58 nm. The mean nanoparticles diameter is 38 nm with a standard deviation of 5 nm.

The average particle size and size distribution of sample N2 was also characterized by scanning electron microscope. Fig. 3.3 shows a SEM image of sample N2 and its corresponding histogram of size distribution is presented in Fig. 3.6. The histogram reveals that sample N2 nanoparticles also have a broad size distribution as well, between 17 and 33 nm. The mean nanoparticles diameter is 27 nm with a standard deviation of 4 nm, smaller than that of sample N1.

3.2.2 AFM Results

Atomic force microscope(AFM) measurements were also performed in order to check the size of YAG:Ce^{3+} nanoparticles by using a Dimension^{TM} 3100 Scanning Probe Microscope (SPM), in the AFM's tapping mode. The AFM produced high–resolution, three–dimensional (x, y and z) images by scanning a sharp tip over the sample surface. Fig. 3.7 shows a typical AFM image of sample N1. The results of sample N2 were similar to those of sample N1. As in SEM images, the nanoparticles showed evidence of the formation of clusters. It is difficult to distinguish individual nanoparticles in the interior of the clusters where the nanoparticles are dense. However, distinct particles could be found between the large clusters on the

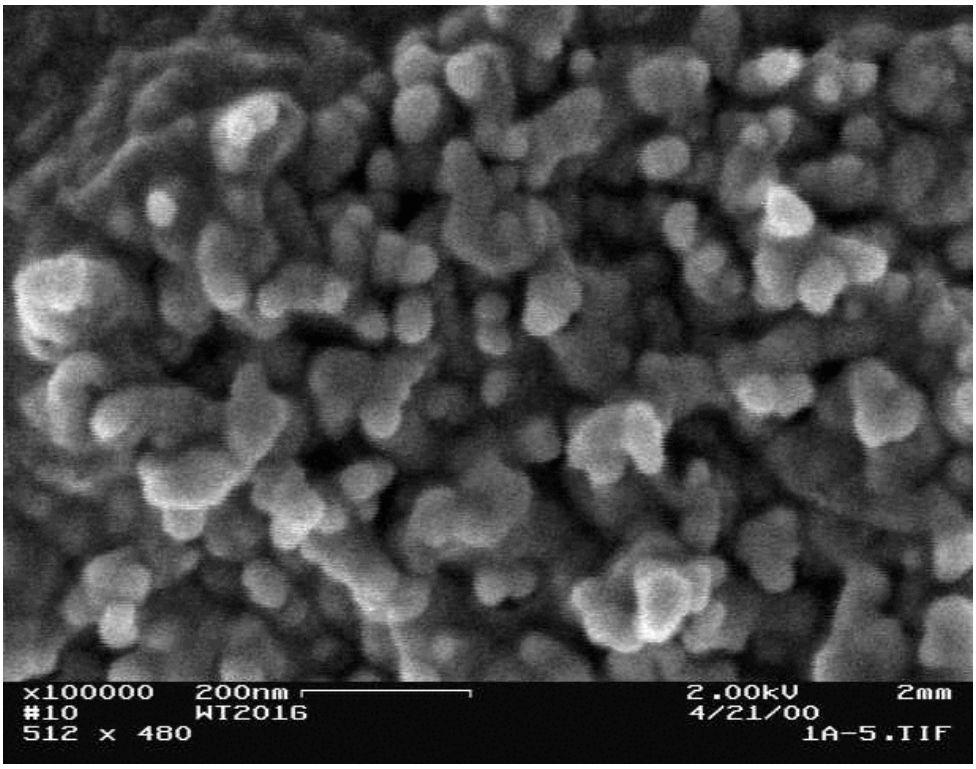

Figure 3.3: SEM image of YAG:Ce^{3+} nanoparticles (N1).

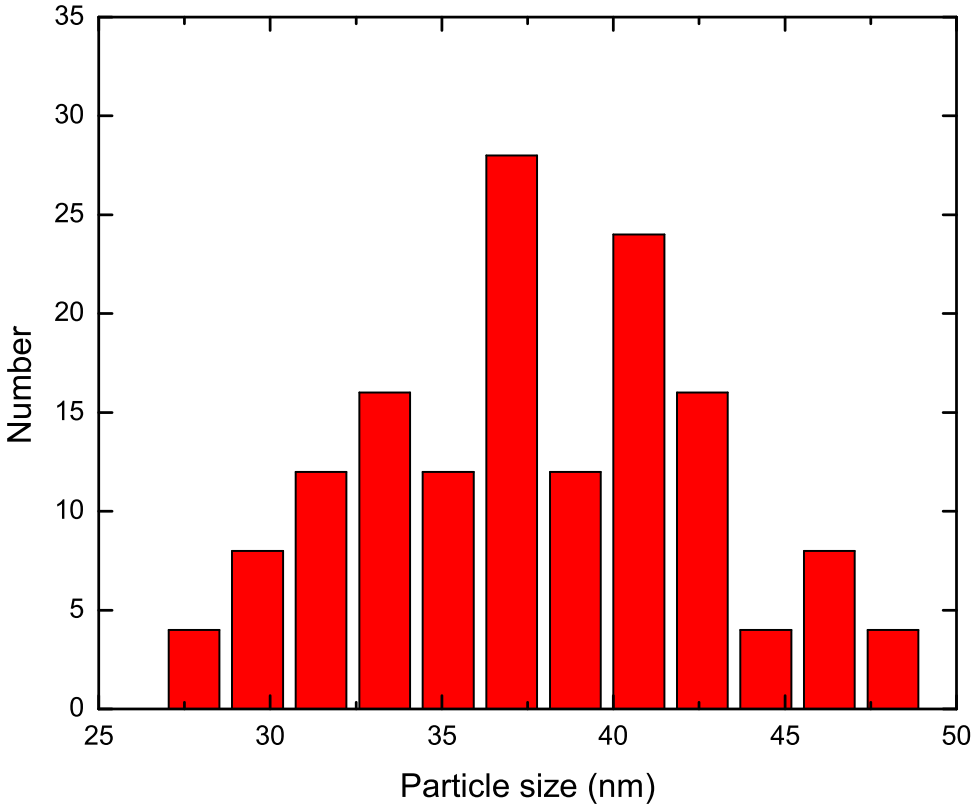

Figure 3.4: The size distribution of YAG:Ce^{3+} nanoparticles (N1). The mean size is 38 nm, and the standard deviation is 5 nm.

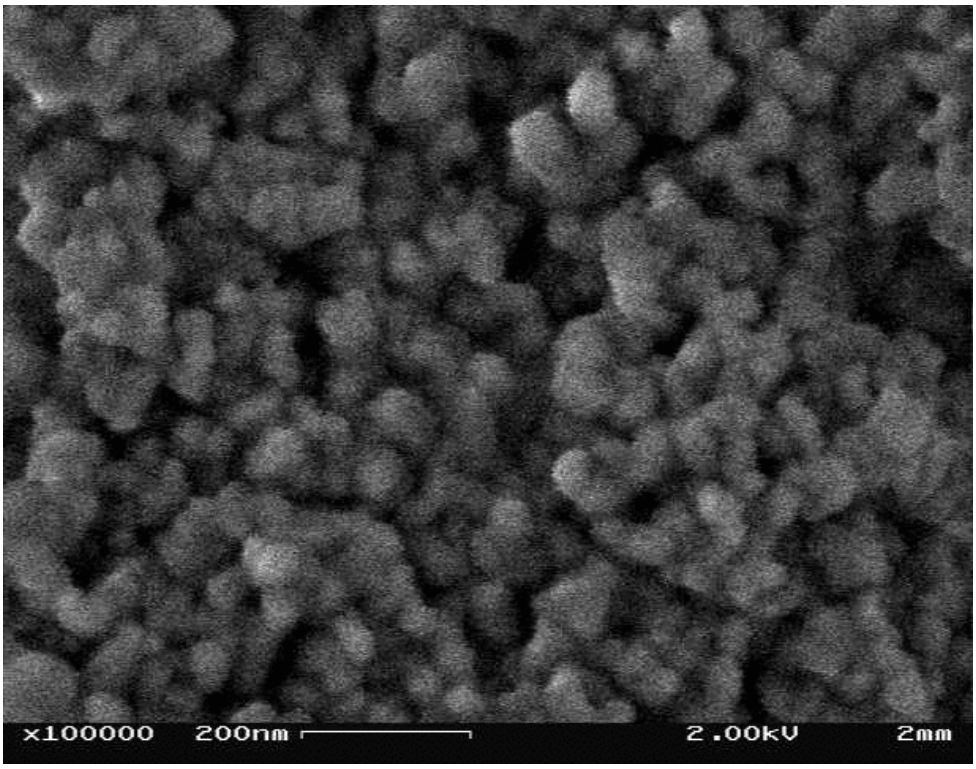

Figure 3.5: SEM image YAG:Ce^{3+} nanoparticles (N2).

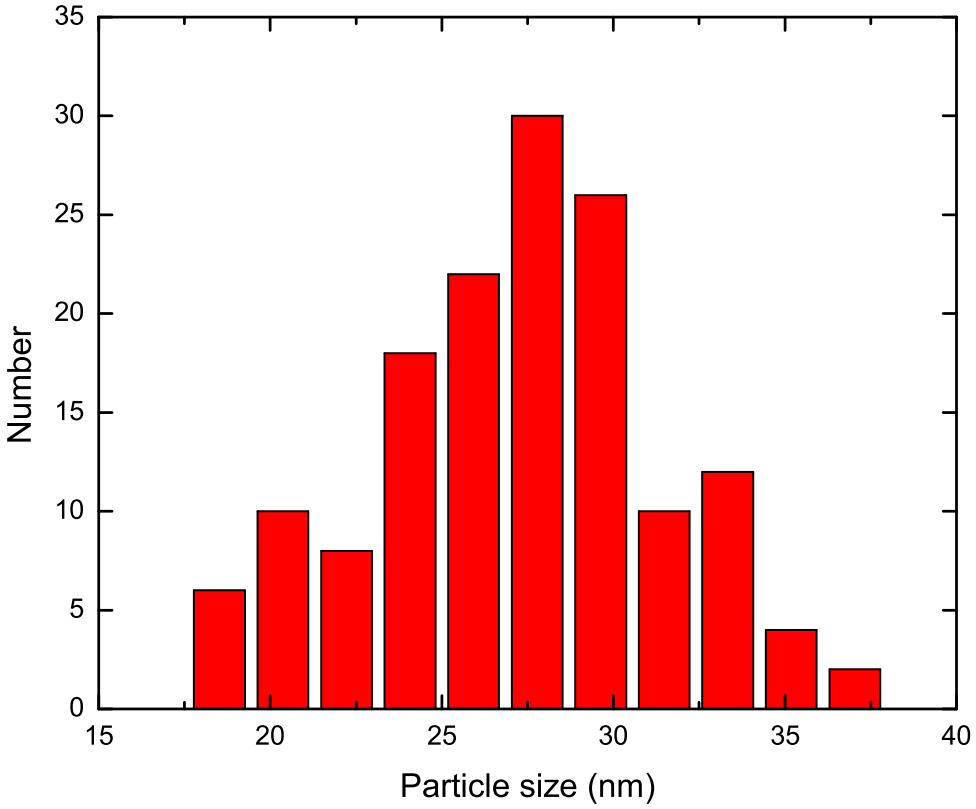

Figure 3.6: The size distribution of sample $N2$ of YAG:Ce^{3+} nanoparticles used in this work. The mean size is 27 nm, and the standard deviation is 4 nm.

surface of the sample holder. The particle size of the YAG:Ce^{3+} nanoparticles was determined by performing a section analysis, and the results were consistent with those obtained using the SEM. Both nanoparticle samples, sample N1 and sample N2, show particles where the average size was 25∼35 nm and aggregates where the average size was considerably larger, a number of somewhat smaller nanoparticles, were also observed.

3.2.3 TEM Results of Sample L1

Fig. 3.8 show a TEM image of nanoscale YAG:Ce^{3+} taken from the paper Q. Li, L. Gao and D. Yan, Mater. Chem. & Phys., **10**, (1998) 2837–2845. This material was prepared using the polyacrylamide gel method. Since the Authors' did not state the particle size and size distribution, Fig. 3.8 was used to generate the size distribution shown in Fig. 3.9 using the approach described above. The data in Fig. 3.9 indicates a particle size of 130 ± 38 nm.

3.3 Excitation and Emission Spectra Measurements

3.3.1 Experimental Setup and Apparatus

Room temperature excitation and emission spectra for both sets of samples, YAG:Ce^{3+} nanoparticles and bulk materials, were taken and compared with each other. An ISA–SPEX FluroMax–2 spectrofluorometer was used to perform the excitation spectra measurements. A simplified block diagram of the spectrofluorometer is shown in Fig. 3.10.

The ISA-SPEX FluoroMax–2 spectrofluorometer uses a 150W continuous xenon lamp as the light source and two modified Czerny–Turner monochromators in both the excitation and emission paths. Light from the xenon lamp enters the excitation monochromator, is spectrally filtered and directed into the sample compartment. 8%

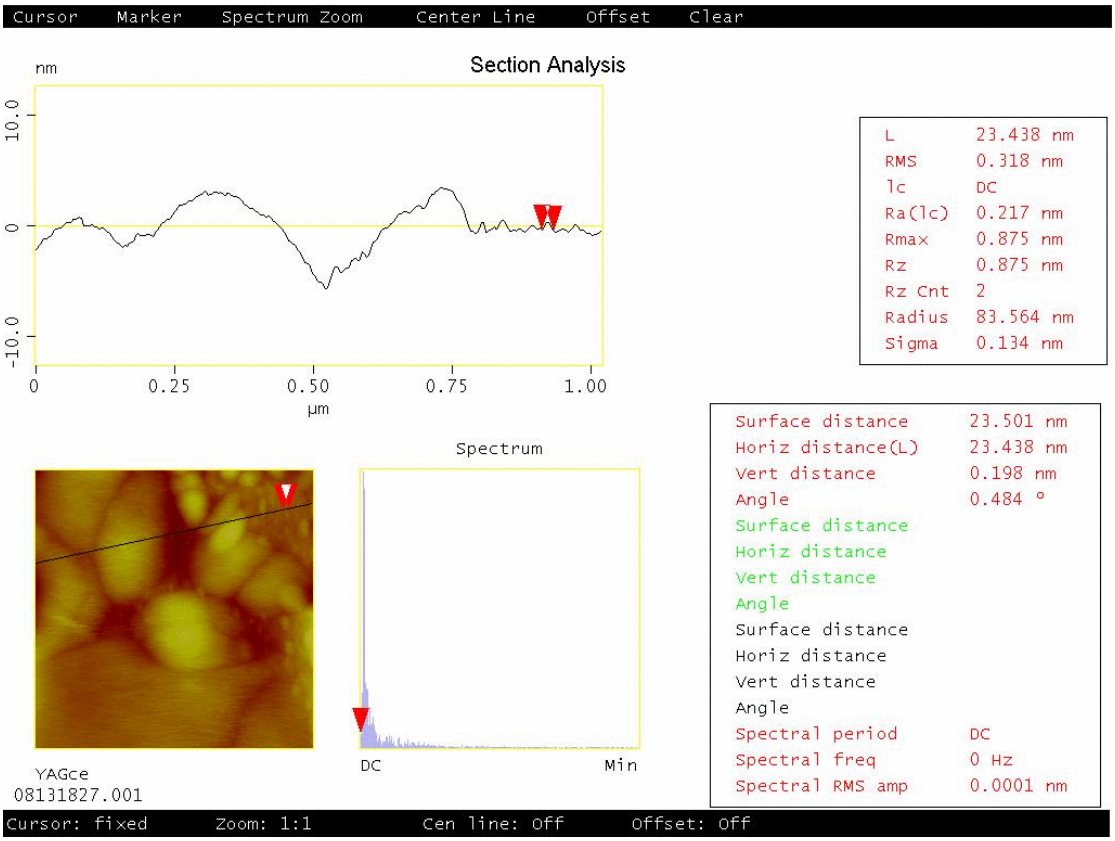

Figure 3.7: AFM image and section analysis of sample N1 of YAG:Ce^{3+} nanoparticles.

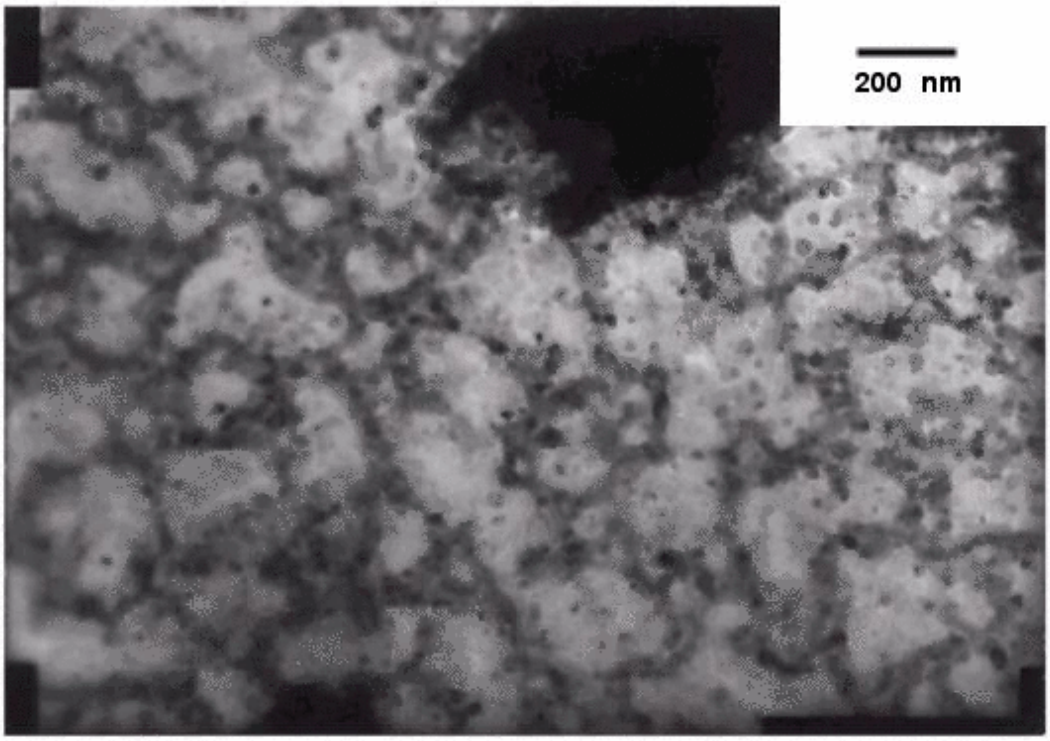

Figure 3.8: TEM image of YAG:Ce^{3+} nanoparticles. This picture is from Q. Li, L. Gao and D. Yan, Mater. Chem. & Phys., **10**, (1998) 2837–2845

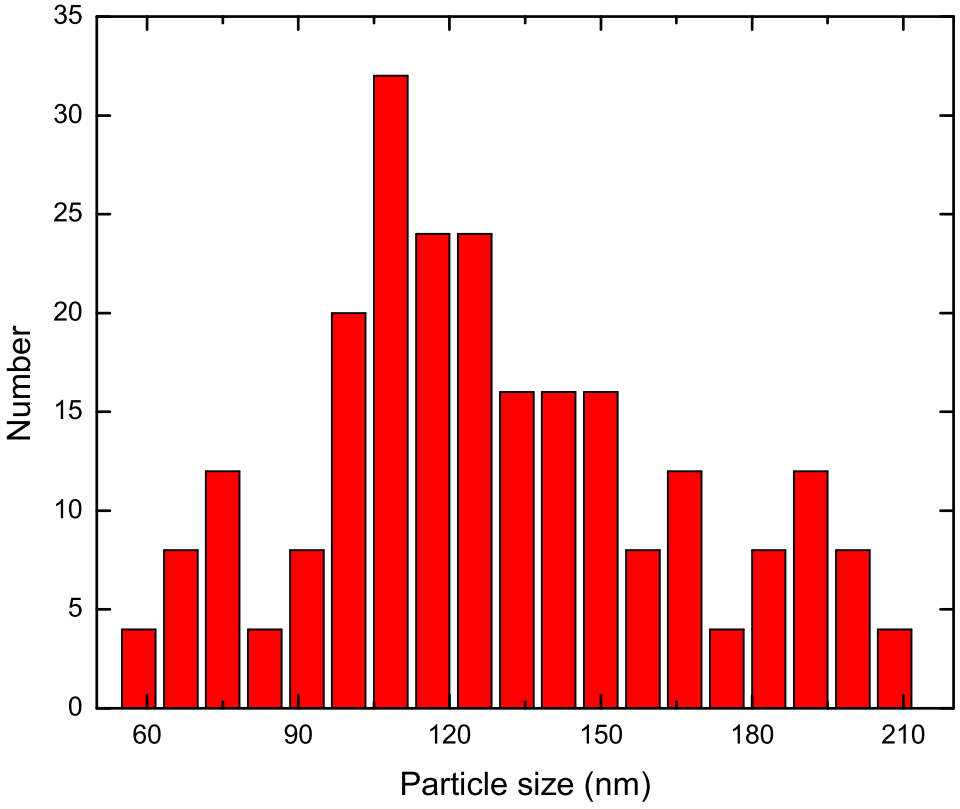

Figure 3.9: The size distribution of YAG:Ce^{3+} nanoparticles in the paper of Q. Li, L. Gao and D. Yan, Mater. Chem. & Phys., **10**, (1998) 2837–2845.. The mean size is 130 nm, and the standard deviation is 38 nm.

of the light is directed onto a reference photo diode using a quartz beam–splitter. Fluorescence from the sample is then collected and directed to the emission monochromator, spectrally filtered and detected by a signal photomultiplier detector. Data is collected using single photon counting. By ratioing the fluorescence signal to a reference signal, correction can be made for variations in the lamp intensity as a function of wavelength.

The measurements of fluorescence spectra utilized a frequency tripled Q–switched Nd:YAG laser (Spectra–Physics' Quanta–Ray DCR–11) as the excitation source. A schematic diagram of the experimental set up is shown in Fig. 3.11. The laser beam is focused onto the samples at a 60^o angle of incidence in order to reduce the effect of laser scatter. Nanoparticle sized powders were specially mounted in small wells which were machined into a brass sample holder with a diameter of 1.5 mm and a depth 0.5 mm. The samples were held in place by a BK7 glass window which also provided optical access. A collimating lens was used to collect the fluorescence. The fluorescence is filtered by a UV blocking filter and a Jobin Yvon/Spex Model 340 single grating monochromator. The signal from an RCA C32034 photomultiplier tube (PMT) was amplified by a Phillips 100× Amplifier and input to a Stanford Research SR400 gated photon counter. Data was collected using a microcomputer. Care was taken to calibrate both experimental setups using known spectral lines.

All the excitation spectra were monitored at 18862 cm^{-1}, and emission were excited at 28161 cm^{-1}.

3.3.2 Experimental Results

Excitation spectra measurements are presented in Figs. 3.12 through 3.15, corresponding to sample N1, N2, B1, and B2 respectively. The data has been converted to wavenumbers (in vacuum) using a value for the refractive index of air, $n_{air} = 1.0003$ The excitation spectra show two prominent features, both of which correspond to

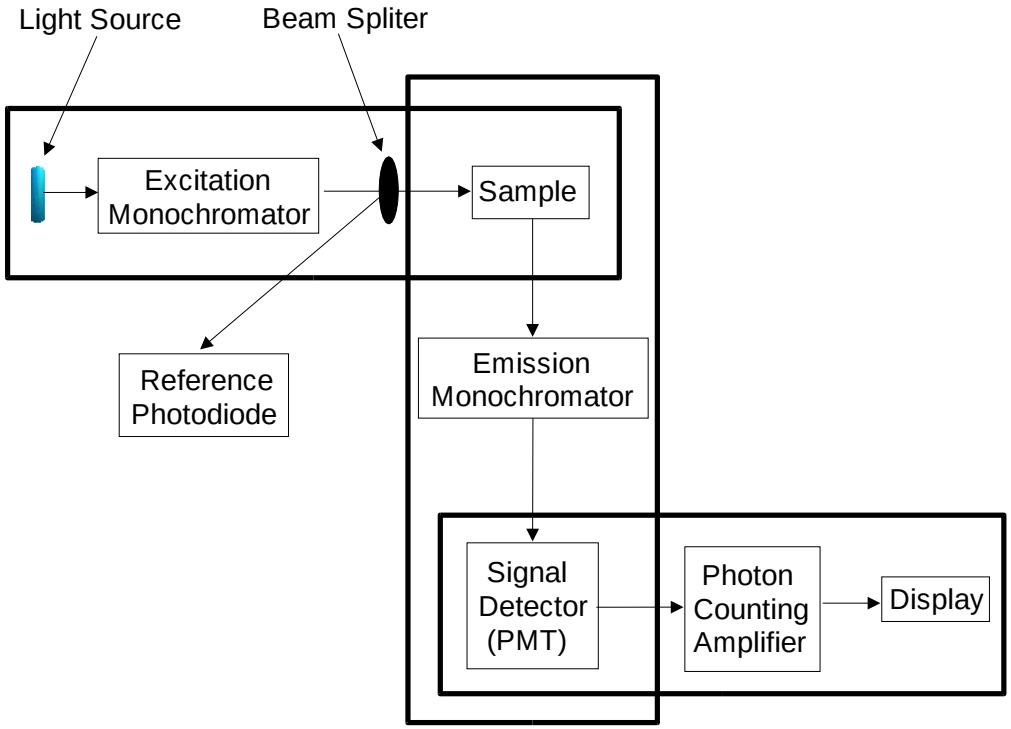

Figure 3.10: Simplified block diagram of a SPEX FluroMax–2 spectrofluorometer.

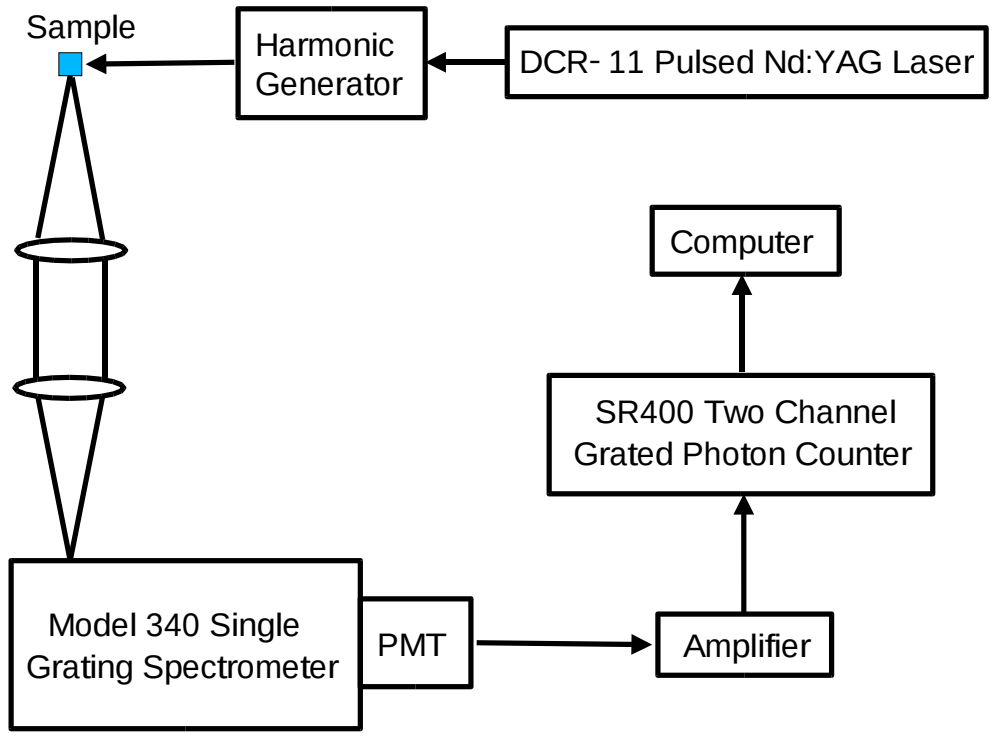

Figure 3.11: Schematic diagram of the experimental setup used for fluoroscence measurements.

Table 3.1: Comparison of the excitation frequency of YAG:Ce^{3+} nanoparticles and those of bulk YAG:Ce^{3+}.

	Excitation peak 1 (cm^{-1})	Excitation peak 2 (cm^{-1})
N1	21834 ± 1	295351 ± 1
N2	21833 ± 1	29533 ± 1
B1	21939 ± 89	29104 ± 1
B2	21974 ± 1	29393 ± 1
L1	21800 ± 1	28979 ± 1

excitation features reported in the literature[1]. The lower frequency peak is the most intense of the excitation peaks. The peaks in the excitation spectra are due to transitions from the ground state to the first two crystal field split $5d$ states.

Since the electron–lattice coupling is strong, the expected Pekarian lineshape is well approximated by a Gaussian function. The data was therefore fit to the sum of Gaussian functions

$$I(\nu) = \sum_i A_i \exp\left[-\left(\frac{\nu - \nu_i}{\delta\nu_i}\right)^2\right] \tag{3.1}$$

where A_i, ν_i and $\delta\nu_i$ are the amplitude, position and width of peak i, respectively and $i = 1, 2$. The fitting process was repeated five times for each spectrum, the results averaged and the standard deviation calculated. The peak position obtained from the above fitting procedure are tabulated in Table 3.1.

The excitation data of Li and co–workers[1] on another YAG:Ce^{3+} nanoscale material was digitized from their paper (see Fig. 3.16) and fit using the same procedure as above. The peak positions for this data is also presented in Table 3.1.

Fluorescence spectra corresponding to the excitation spectra described above are shown in Figs. 3.17 through 3.21. The emission spectra of all the samples have a sim-

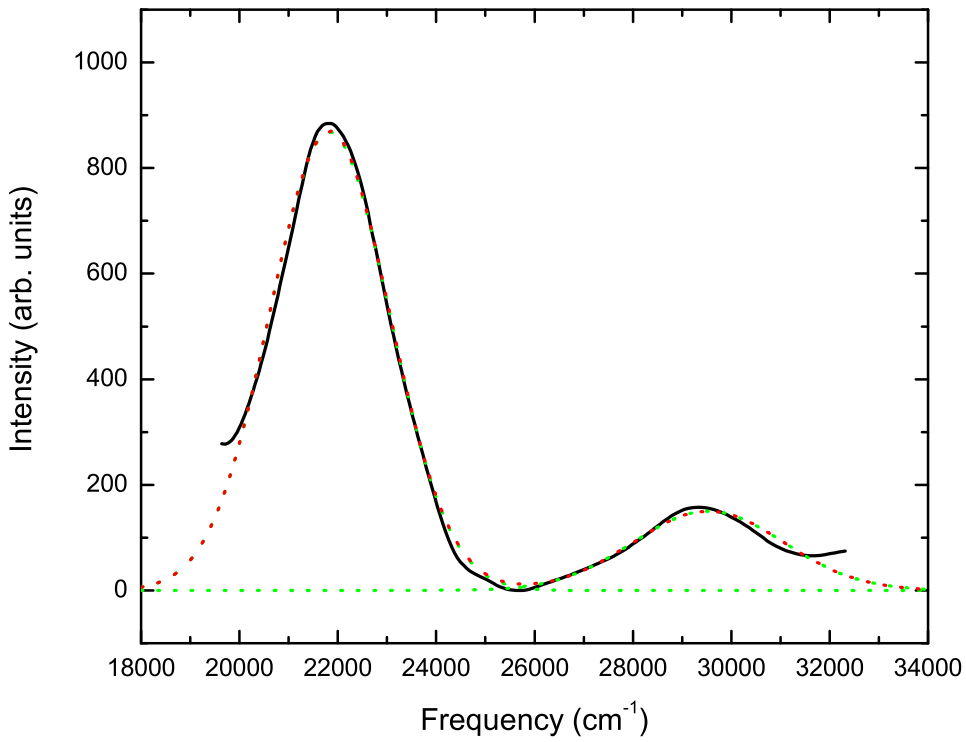

Figure 3.12: Room temperature excitation spectrum and the fit to two Gaussian functions for YAG:Ce^{3+} nanoparticles (N1). The excitation spectrum was monitored at 18862 cm^{-1}. The solid line is experimental data. The dashed line is the fitted curve.

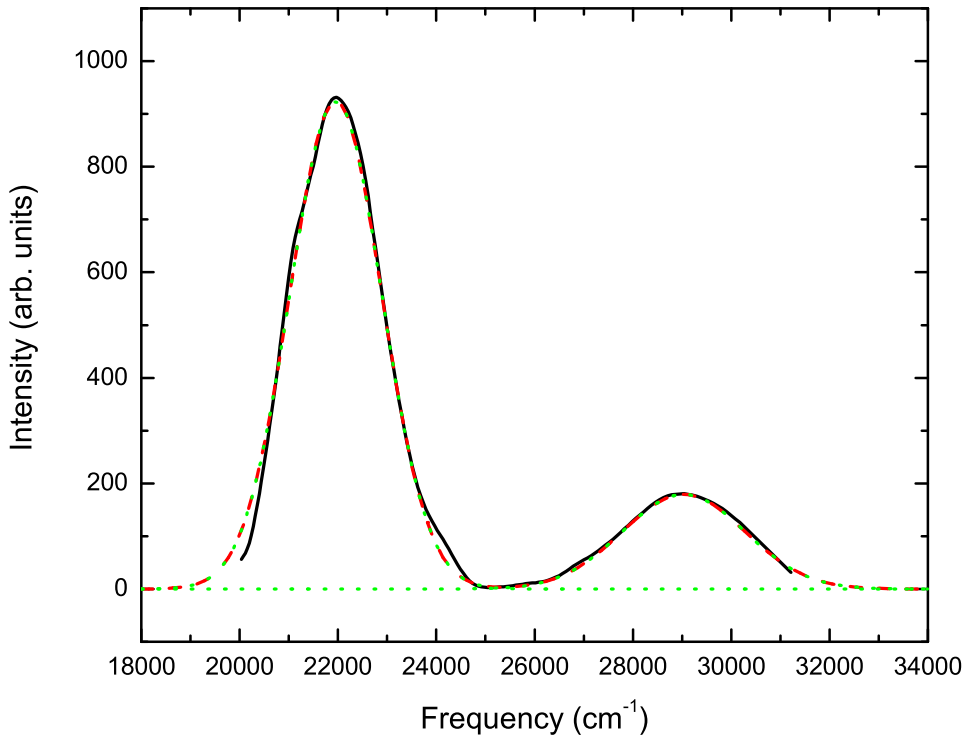

Figure 3.13: Room temperature excitation spectrum and the fit to two Gaussian functions for YAG:Ce^{3+} nanoparticles (N2). The excitation spectrum was monitored at 18862 cm^{-1}. The excitation spectrum was observed at 18862 cm^{-1}. The solid line is experimental data. The dashed line is the fitted curve

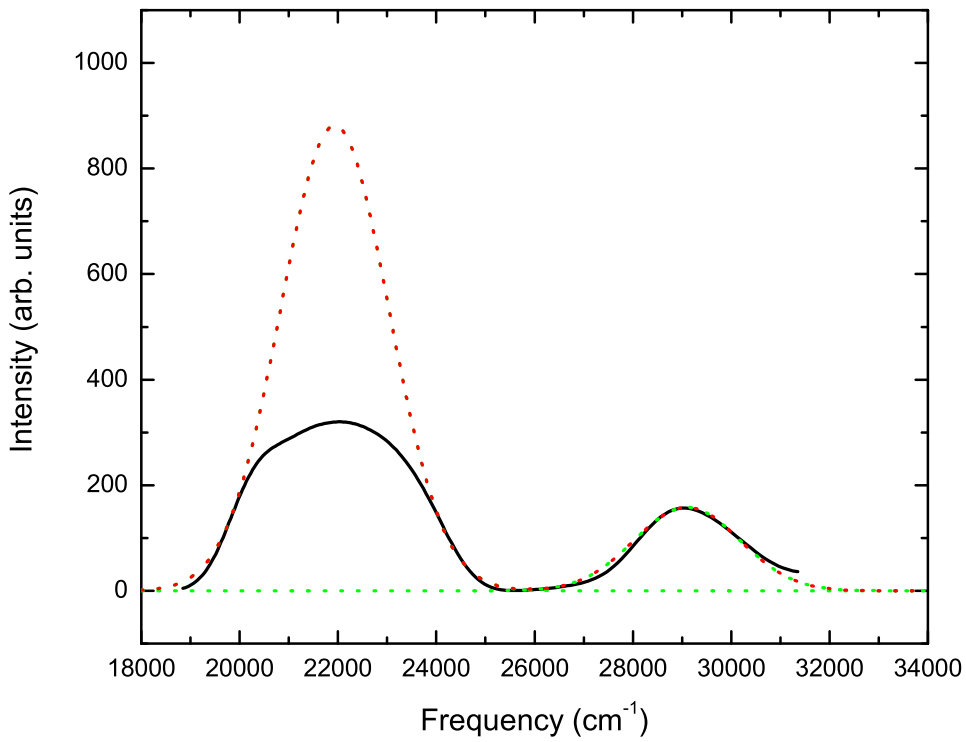

Figure 3.14: Room temperature excitation spectrum and the fit to two Gaussian functions for YAG:Ce^{3+} fused crystalline material (B1). The excitation spectrum was observed at 18862 cm^{-1}. The excitation spectrum was monitored at 18862 cm^{-1}. The solid line is experimental data. The dashed line is the fitted curve. The low frequency peak appears to be saturated due to a high Ce^{3+} concentration in this sample.

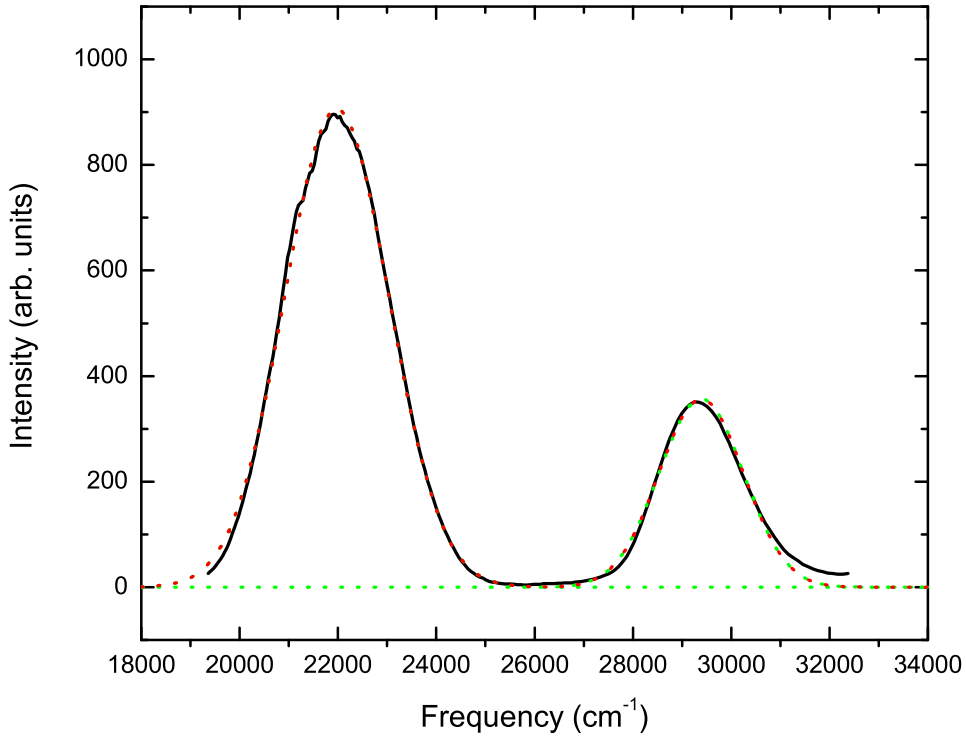

Figure 3.15: Room temperature excitation spectrum and the fit to Gaussian functions for the YAG:Ce^{3+} single crystal fiber (B2). The excitation spectrum was monitored at 18862 cm^{-1}. The solid line is experimental data. The dashed line is the fitted curve.

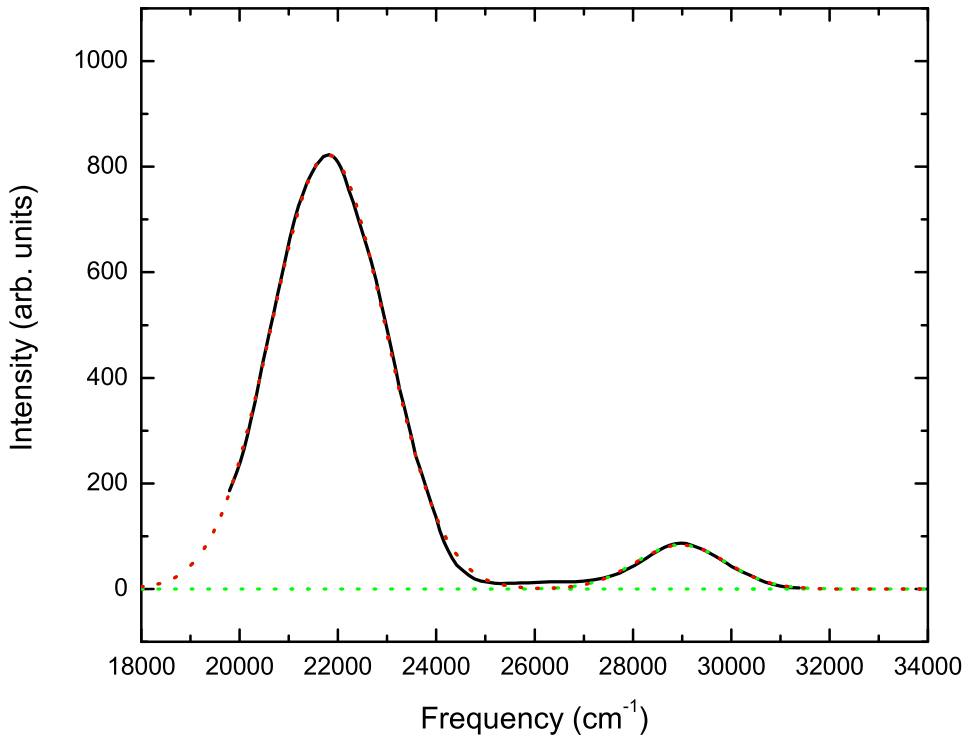

Figure 3.16: Room temperature excitation spectrum and the fit to two Gaussian functions for YAG:Ce^{3+} nanoparticles (L1) from Q. Li, L. Gao and D. Yan, Mater. Chem. & Phys., **10**, (1998) 2837–2845. The excitation spectrum was observed at 18862 cm^{-1}. The solid line is experimental data. The dashed line is the fitted curve.

Table 3.2: Comparison of the excitation frequency of YAG:Ce^{3+} nanoparticles and those of bulk YAG:Ce^{3+}. * means the data were taken using the FluoroMax–2 spectrofluorometer.

	Emission peak 1 (cm^{-1})	Emission peak 2 (cm^{-1})
N1	17188 ± 94	19126 ± 28
N2	16960 ± 184	19138 ± 182
B1	17438 ± 90	19101 ± 67
B1*	17819 ± 9	19150 ± 3
B2*	17379 ± 1	19124 ± 1
L1	17540 ± 2	19039 ± 1

ilar shape, and match the spectral features reported in the literature for YAG:Ce^{3+}. The main features of the emission spectra consist of a broad band (with a shoulder) in the green. This is due to emission of the Ce^{3+} ion which originates from the lowest $5d$ level to the $^2F_{5/2}$ and $^2F_{7/2}$ levels.

When it was attempted to measure the fluorescence spectra of the nanoparticles using a continuous working lamp source (Fluoromax–2) at 355 nm, the fluorescence was too weak to be measured effectively. To overcome this problem fluorescence spectra were measured using the experimental setup in Fig. 3.11. A comparison of spectra taken on bulk YAG:Ce^{3+} using both techniques is given in Fig. 3.19 and Fig. 3.20. The experimental data along with the digitized data of Li and co–workers was fit to the sum of two or three Gaussians using the same procedure as above (see Fig. 3.22)[1]. The results are tabulated in Table 3.2.

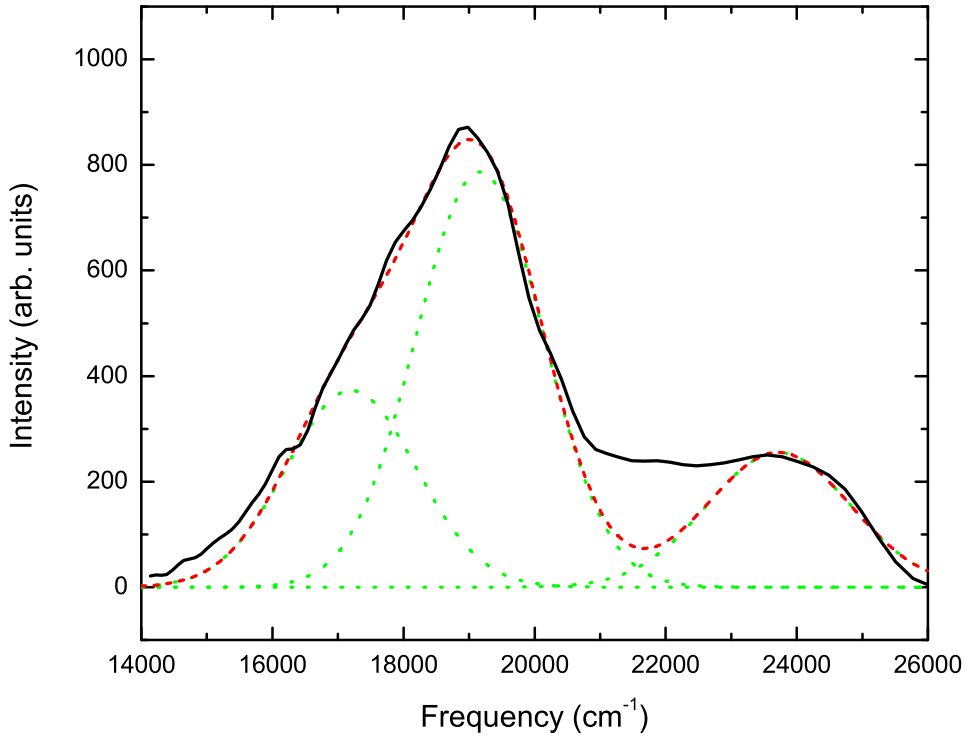

Figure 3.17: Room temperature emission spectrum and the fit to three Gaussian functions for YAG:Ce^{3+} nanoparticles (N1). The emission spectrum was excited at 28161 cm^{-1}. The solid line is the average of the experimental data. The dashed line is the fitted curve and the dotted lines are the individual Gaussian fits.

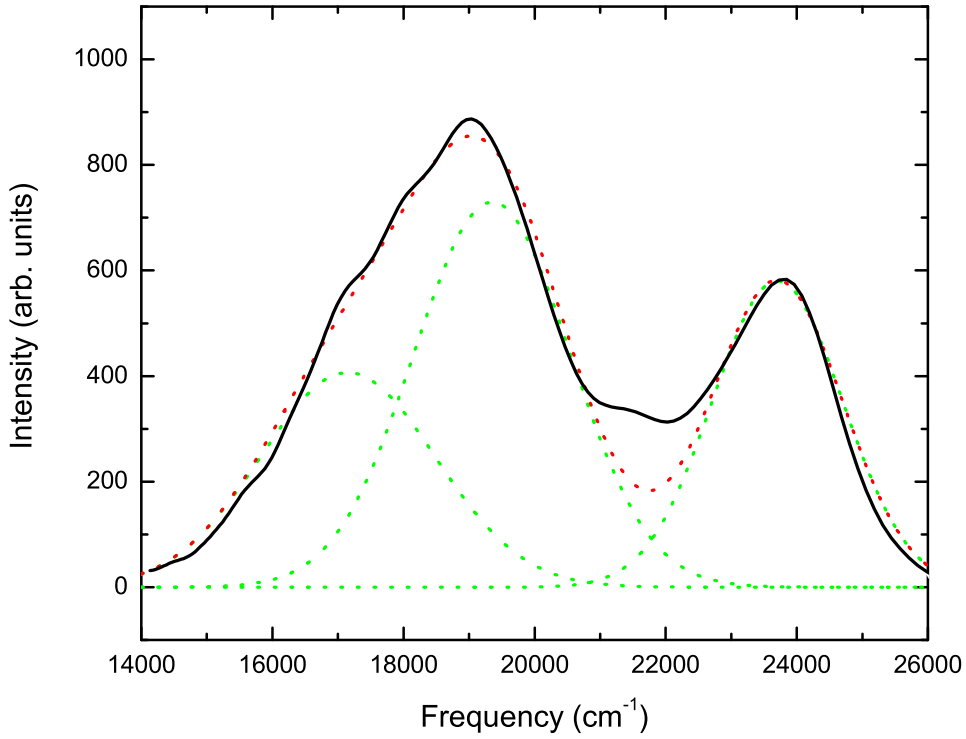

Figure 3.18: Room temperature emission spectrum and the fit to three Gaussian functions for YAG:Ce^{3+} nanoparticles (N2). The emission spectrum was excited at 28161 cm^{-1}. The solid line is the average of the experimental data. The dashed line is the fitted curve and the dotted lines are the individual Gaussian fits.

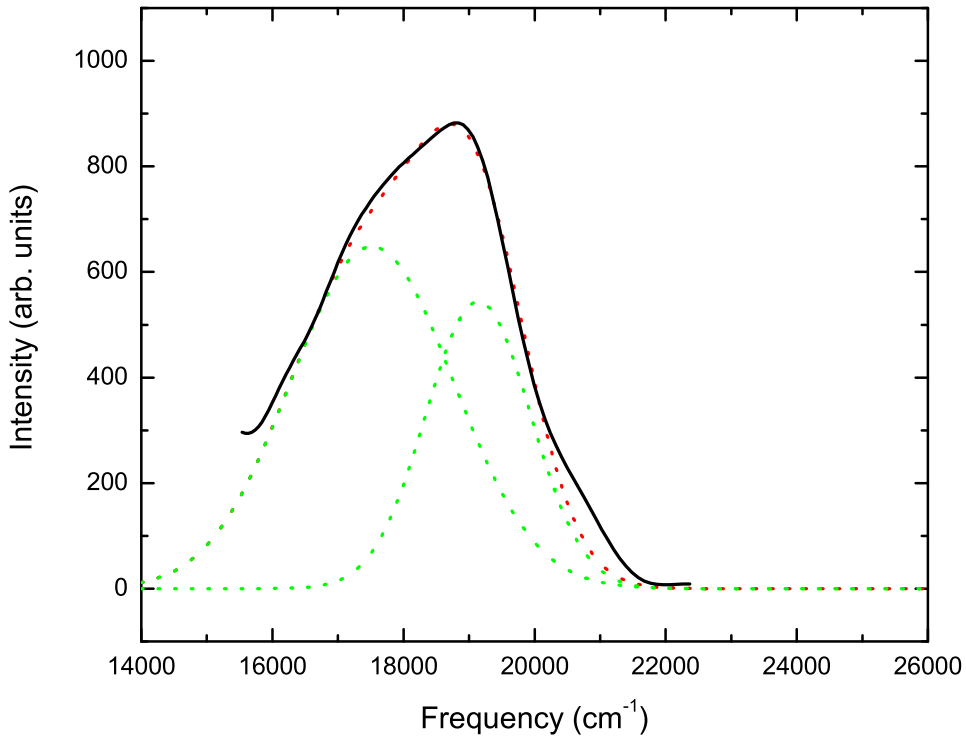

Figure 3.19: Room temperature emission spectrum and the fit to two Gaussian functions for YAG:Ce^{3+} fused crystalline material (B1). The emission spectrum was excited at 37583 cm^{-1} using a FluroMax–2 spectrofluorometer shown in Fig. 3.10. The solid line is the average of the experimental data. The dashed line is the fitted curve and the dotted lines are the individual Gaussian fits.

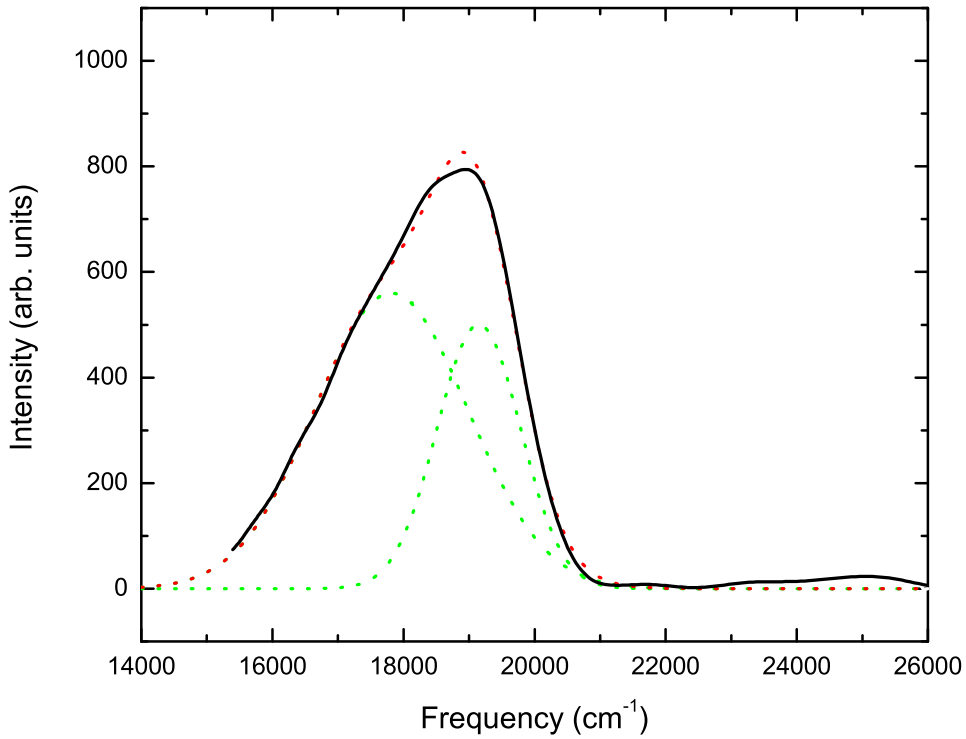

Figure 3.20: Room temperature emission spectrum and the fit to two Gaussian functions for YAG:Ce^{3+} fused crystalline material (B1). The emission spectrum was excited at 28161 cm^{-1} using the experimental setup shown in Fig. 3.11. The solid line is the average of the experimental data. The dashed line is the fitted curve and the dotted lines are the individual Gaussian fits.

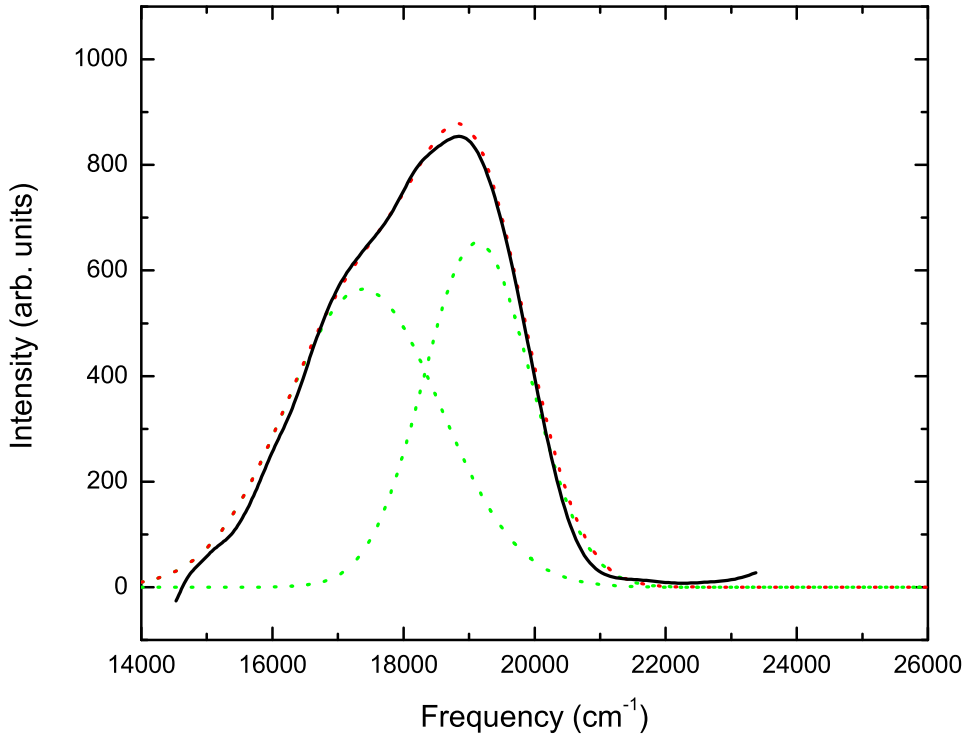

Figure 3.21: Room temperature emission spectrum and the fit to two Gaussian functions for YAG:Ce^{3+} single crystal fiber (B2). The emission spectrum was excited at 28161 cm^{-1}. The solid line is the average of the experimental data. The dashed line is the fitted curve and the dotted lines are the individual Gaussian fits.

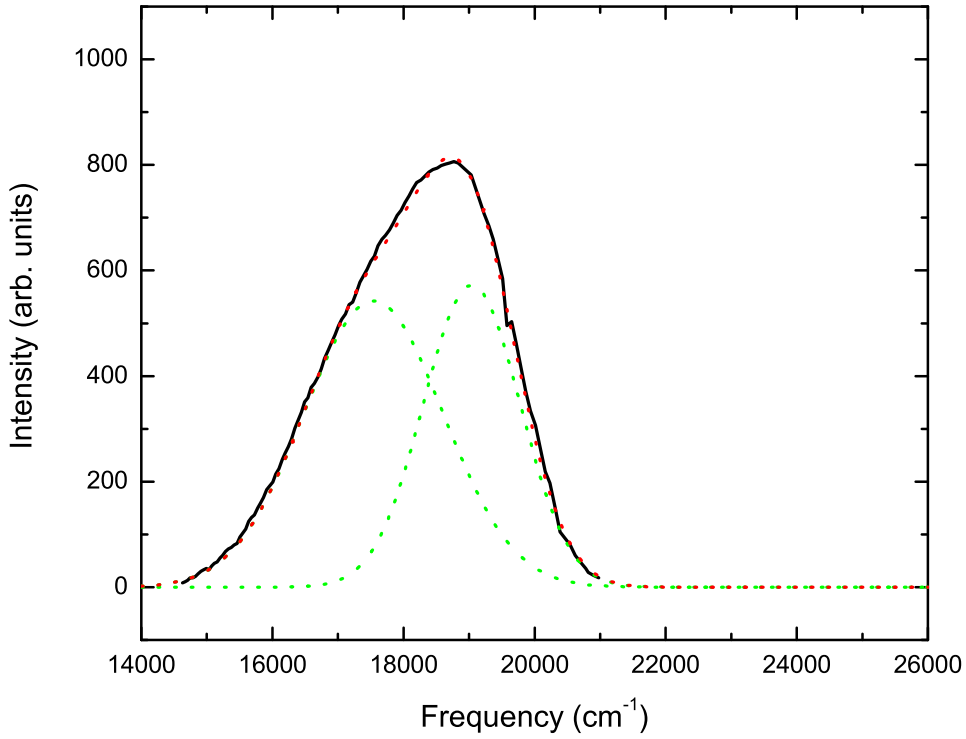

Figure 3.22: Room temperature emission spectrum and the fit to Gaussian functions for YAG:Ce^{3+} nanoparticles reported in the literature[1]. The solid line is the average of the digitized data. The dashed line is the fitted curve and the dotted lines are the individual Gaussian fits.

3.4 Discussion

The similarity between the excitation and emission spectra of the bulk and nanoparticle materials strongly indicate that the nanoparticles are crystalline YAG:Ce^{3+} since the position of the $5d$ states with respect to the $4f$ ground state is strongly crystal field and hence host dependent.

Li and co–workers reported a spectral blue shift in going from bulk to nanoscale YAG:Ce^{3+}[1]. In order to check this result in the samples used in this thesis. The data from Table 3.1 and Table 3.2 was used.

The data for both nanoparticles (N1 and N2) was averaged as was the data for the bulk materials, B1 and B2 in excitation and B1, B1* and B2 in emission. The following averaged quantities were calculated:

$$\Delta\nu_L^{EX} = \nu_{L,NANO}^{EX} - \nu_{L,BULK}^{EX} \tag{3.2}$$

$$\Delta\nu_H^{EX} = \nu_{H,NANO}^{EX} - \nu_{H,BULK}^{EX} \tag{3.3}$$

$$\Delta\nu_L^{EM} = \nu_{L,NANO}^{EM} - \nu_{L,BULK}^{EM} \tag{3.4}$$

$$\Delta\nu_H^{EM} = \nu_{H,NANO}^{EM} - \nu_{H,BULK}^{EM} \tag{3.5}$$

where ν is the frequency. EX stands for excitation, and EM stands for emission. L refers to the low frequency peak and H refers to the high frequency peak. The following values were calculated.

$$\Delta\nu_L^{EX} = -123 \pm 89 \tag{3.6}$$

$$\Delta\nu_H^{EX} = 286 \pm 2 \tag{3.7}$$

$$\Delta\nu_L^{EM} = -471 \pm 226 \tag{3.8}$$

$$\Delta\nu_H^{EM} = 7 \pm 196 \tag{3.9}$$

The results show that the splitting between the two $5d$ levels is enlarged, which suggests the cubic distortion in the nanoparticle YAG:Ce^{3+} is increased. We point out that the spectral shifts observed in this thesis are opposite to those observed by Li and co–workers[1], therefore, at this time we do not belive te evidence of a spectral shift due to finite size effects to be conclusion. In order to obtain larger spectral shift in nanoparticle YAG:Ce^{3+}, the size of the nanoparticles should be smaller, generally less than 10 nm when the high surface to volume ratio should cause larger modifications to the crystal field at the Ce^{3+} site.

3.5 References

[1] Q. Li, L. Gao and D. Yan, Mater. Chem. & Phys., **10**, (1998) 2837–2845.

[2] B. M. Tissue, Chem. Mater., **10**, (1998) 2837–2845.

Chapter 4

Conclusions

Ce^{3+} doped YAG nanoparticles has been prepared and characterized. Scanning electron microscopy was performed on particles collected from both the cold finger (sample N1) and the sample chamber walls (sample N2). The SEM image of the nanoparticles used in this study reveals that the nanoparticles powder forms three–dimensional clusters of nanoscaled crystallites and with a broad size distribution. Size distributions were calculated for both sets of samples. Both samples showed aggregates where the average sample size was 30$\sim$40 nm, however aggregates where the average size was considerably larger (and somewhat smaller) were also observed. Atomic force microscopy (AFM) measurements were also performed and the results were consistent with the SEM results.

The excitation and emission spectra of the nanoparticles were compared to those of the two bulk samples, as well as a YAG:Ce^{3+} nanoscale material reported in literature[1]. Both excitation and emission spectra for the nanoparticles were very similar to those for the bulk materials indicating that the nanoparticles prepared using gas–phase condensation technique are indeed YAG:Ce^{3+} nanocrystals.

The spectral blue shift reported by Li and coworkers[1] was not reproduced. Future work would include investigating spectral shifts in significantly smaller YAG:Ce^{3+} nanoparticles, i.e. particles with diameters $\leq$ 10 nm as the higher surface to volume ratio should cause a larger modification to the crystal field at the Ce^{3+} site.

4.1 References

[1] Q. Li, L. Gao and D. Yan, Mater. Chem. & Phys., **10**, (1998) 2837–2845.